Research Article

Nanoscale Charge Accumulation and Its Effect on Carrier Dynamics in Tri-cation Perovskite Structures

David Toth, Bekele Hailegnaw, Filipe Richheimer, Fernando A. Castro, Ferry Kienberger, Markus C. Scharber, Sebastian Wood, and Georg Gramse*

Cite This: ACS Appl. Mater. Interfaces 2020, 12, 48057−48066

Read Online

ACCESS | Metrics & More | Article Recommendations | Supporting Information

ABSTRACT: Nanoscale investigations by scanning probe microscopy have provided major contributions to the rapid development of organic−inorganic halide perovskites (OIHP) as optoelectronic devices. Further improvement of device level properties requires a deeper understanding of the performance-limiting mechanisms such as ion migration, phase segregation, and their effects on charge extraction both at the nano- and macroscale. Here, we have studied the dynamic electrical response of $Cs_{0.05}(FA_{0.83}MA_{0.17})_{0.95}PbI_{3−x}Br_x$ perovskite structures by employing conventional and microsecond time-resolved open-loop Kelvin probe force microscopy (KPFM). Our results indicate strong negative charge carrier trapping upon illumination and very slow (>1 s) relaxation of charges at the grain boundaries. The fast electronic recombination and transport dynamics on the microsecond scale probed by time-resolved open-loop KPFM show diffusion of charge carriers toward grain boundaries and indicate locally higher recombination rates because of intrinsic compositional heterogeneity. The nanoscale electrostatic effects revealed are summarized in a collective model for mixed-halide CsFAMA. Results on multilayer solar cell structures draw direct relations between nanoscale ionic transport, charge accumulation, recombination properties, and the final device performance. Our findings extend the current understanding of complex charge carrier dynamics in stable mulication OIHP structures.

KEYWORDS: perovskite, nanoscale, charge-dynamics, optoelectronics, photovoltaics, scanning probe microscopy, kelvin probe force microscopy
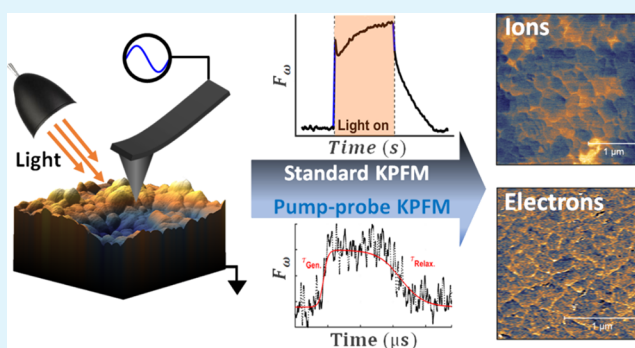
INTRODUCTION

In the last decade, organic−inorganic halide perovskites (OIHPs) have received tremendous attention for optoelectronic applications, which has triggered rapid scientific progress in this field.[1,2] In particular, single-junction OIHP photovoltaic devices have reached efficiencies of ∼25%, open circuit voltages >1.2 V and short circuit currents >20 mA cm^{-2}.[3,4] Further advancement toward the Shockley−Queisser limit requires a comprehensive micro- and macroscale understanding of performance-limiting effects, such as ionic migration and phase segregation in OIHPs. Defect formation via these processes can lead to the creation of nonradiative recombination pathways that result in spatially inhomogeneous recombination times and energetically preferred recombination sites.[5−7] In typical I−Br mixed-halide perovskites, iodide- and/or bromide-rich phases tend to form under prolonged illumination.[8,9] Confocal photoluminescence (PL) measurements suggest that these phases form at grain boundaries (GB), where current−voltage curve hysteresis is shown to be increased, further indicating ionic displacement and trap site formation.[6,10−12] On the other hand, Li et al. have observed

higher conductivity at GBs via conductive atomic force microscopy (AFM) arguing that GBs act as conduction pathways rather than recombination sites.[13] Cesium-incorporated perovskites offer an attractive solution, as they have been shown to constrain effects such as phase segregation while maintaining high efficiencies.[14,15] This puts them at the focus of device optimization research. As an example, trication mixed-halide perovskite inverted structures utilizing formamidinium (FA), methylammonium (MA), and Cs cations were reported with increased fill factor, high power conversion efficiencies, and improved charge extraction for a two-layered electron transport material (ETM) arrangement. The cells were prepared as indium tin oxide (ITO)/NiO$_x$/perovskite/[6,6]-phenyl-C61-butyric acid methyl ester (PCBM)/TiO$_x$/Al
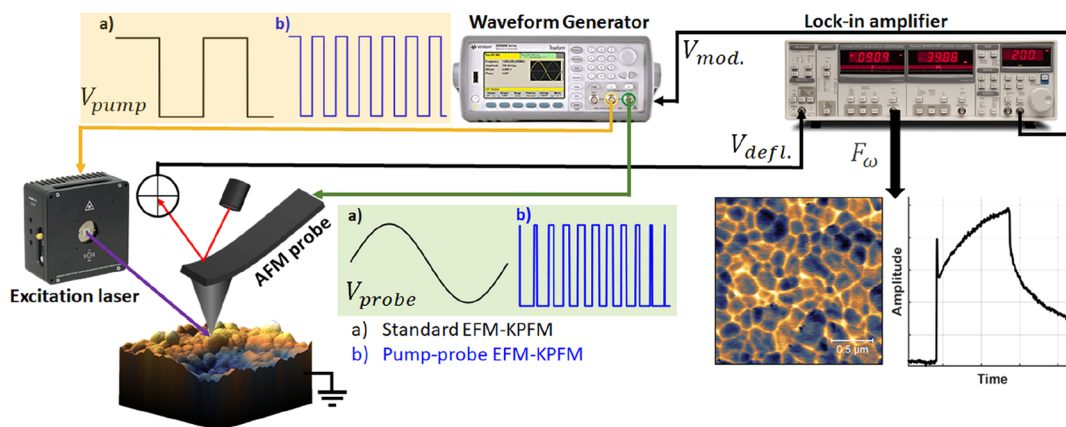
Figure 1. Connection scheme for (a) conventional and (b) pump−probe KPFM measurements. The electrically excited AFM probe is used to characterize the perovskite electrostatic response under illumination.

architectures. The $Cs_{0.05}(FA_{0.83}MA_{0.17})_{0.95}PbI_{3-x}Br_x$ devices with a TiO_x layer on top of the PCBM have shown lower charge carrier extraction resistance via impedance spectroscopy as well as a reduced extent of charge trapping through PL decay measurements compared to devices without the TiO_x layer.[16] Relating these macroscale differences to nanoscale electrical measurements can yield a deeper understanding of the underlying physical behavior.

As recent developments of advanced scanning probe microscopy (SPM) techniques now allow for the characterization of electrically and optically active materials with high temporal resolution, they offer insight into the spatial variation of charge carrier dynamics on multiple timescales.[17−20] These approaches enable noninvasive imaging down to picosecond temporal resolution.[21,22] Improvement of the time resolution has been achieved by various means, such as recording the cantilever deflection read-out signal with ultrahigh sampling rate as well as by overcoming the averaging limitation by applying high-frequency pulses in excitation and detection.[23−26] These approaches have been of particular interest for electrostatic force microscopy (EFM) and Kelvin probe force microscopy (KPFM) applications. The EFM and KPFM techniques rely on the electrostatic force arising between the AFM probe and the sample, separated by a distance z, upon application of an AC voltage. The signal of the detector used for the AFM read-out system is demodulated at the first (F_ω) and/or the second harmonic ($F_{2\omega}$) of the applied AC frequency. While the $F_{2\omega}$ component contains information on the local tip-to-sample capacitance gradient, dC/dz, the F_ω signal also contains information on the contact potential difference (V_{cpd}) between the sample and probe. A feedback loop with an additional DC potential can be applied to the tip in order to extract V_{cpd} from the F_ω signal (closed loop KPFM). Alternatively, in open loop operation, the information from both harmonics can be also combined to separate V_{cpd} and capacitive information. More details on the techniques including voltage conventions can be found in the Methods and Supporting Information Note S1. The so-called pump−probe-based approaches have been used in optical spectroscopy for decades and recently have been applied to electric SPM modes in order to resolve the local decay of the surface photovoltage in organic donor−acceptor blends, V_{cpd} changes in an organic transistor structure with microsecond temporal resolution, and picosecond relaxations of photovoltage in low-temperature grown GaAs.[24,27,28] Limitations and possible

artifacts of this approach have also been investigated by a number of groups.[27,29] Murawski et al. reported on a dual-closed loop system that removes crosstalk artifacts in the topography channel originating from an incorrect voltage applied by the KPFM feedback loop.[28] We overcome this artifact by detecting the first-harmonic signal F_ω directly in open-loop measurements; however, we note that in this case additionally the $F_{2\omega}$ signal has to be considered to separate transient V_{cpd} changes from capacitive changes.

The experimental setup used in this study to investigate both fast and slow charge dynamics on perovskites is shown in Figure 1 and further detailed in the Methods section. The measurements were performed using a 633 nm continuous wave (CW) laser coupled through an electro-optical modulator. The AC voltage applied to the tip was supplied externally, and the demodulation of the detector signal was achieved with an external lock-in amplifier.

In what follows, we investigate the nanoscale spatial differences in the ionic and electronic dynamics of triple-cation mixed halide perovskite photovoltaic structures with results obtained from these two KPFM implementations. We focus first on pristine perovskite films and then discuss results for multilayered samples.

■ RESULTS AND DISCUSSION

Upon optical excitation, the electrostatic force response of a pristine CsFAMAPbBrI perovskite evolves in a complex way at timescales covering several orders of magnitude. This is shown in Figure 2 where we display a typically measured F_ω amplitude response to a ∼10.5 W/cm², 633 nm laser pulse with the dashed lines representing monoexponential fits to separate parts of the curve. Upon illumination, electron−hole pairs are generated with charge carriers accumulating on each side of the perovskite depending on the energy landscape of the structure (step I). The electron mobility has been shown to be in the range of 1−100 cm² V⁻¹ s⁻¹ with characteristic lifetimes of nanoseconds to microseconds for OIHP using techniques such as terahertz electrical conductance.[3] The dynamics of this step is too fast to be resolved by standard EFM techniques. After the electron−hole pair generation, a process takes place on the scale of hundreds of milliseconds (step II). Previous studies have suggested that filling of trap sites via free electronic charge carriers can induce an electric field and subsequent ionic motion.[5,7] Based on this, the formation time of an electric double layer can be described as $\tau_{Debye} = \lambda d/D$, where τ_{Debye} is
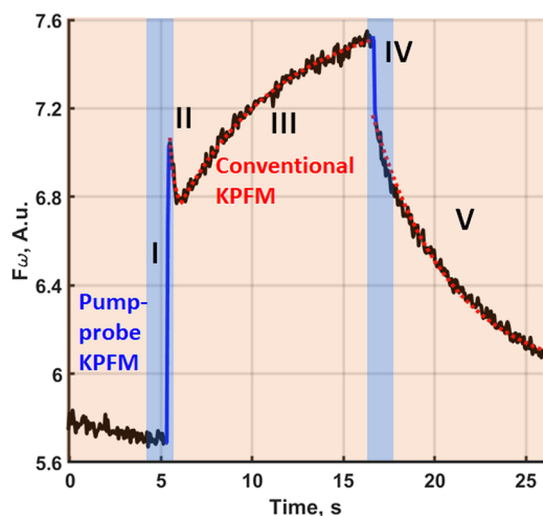
Figure 2. First-harmonic amplitude of the electrostatic force response to a single light pulse (10.5 W/cm², 633 nm) at 10 nm lift height. The distinct dynamical processes are numbered $I-V$. Dashed lines indicate monoexponential fit $(f(x) = y_0 + A\,e^{(x/\tau)})$ of the separate features of the response. Processes in the red region in the second−millisecond range can be accessed by standard KPFM. Fast microsecond dynamics in the blue regions were measured by pump−probe KPFM.

the Debye-time, λ the Debye length, d the film thickness, and D the corresponding diffusion coefficient.[3] Applying this relation with a reported diffusion coefficient of halide ions/

vacancies of $D = 1 \times 10^{-8}$ cm² s⁻¹, the extracted monoexponential time constant $\tau_{II} = 0.23 \pm 0.05$ s and the approximate film thickness $d = 525 \pm 25$ nm yields a Debye-length of $\lambda = 444 \pm 116$ nm.[3] Although the calculated length is reasonable considering the film thickness, this type of analysis does not allow unambiguous attribution to ionic charge carriers. Later on, however, we show that results on multilayer samples support the ionic origin of this step.

Under illumination, an additional process (step III) is recorded, which tends toward a steady value over the course of >10 s ($\tau_{III} = 5.9 \pm 0.2$ s). The dynamics of this process is much slower than the previously described ion/vacancy transport. One possible origin of this process would be halide phase segregation.[30] However, a comparison of the time-evolution of confocal PL spectra recorded at various intensities (see the Supporting Information) excludes this possibility. Figure S1a shows that the PL spectrum measured with 17.5 W/cm² excitation is stable over a period of 90 s with the spectral peak at ∼757 nm. In Figure S1b, we show that the PL peak spectral position remains stable over time for low excitation intensities. Only above around 5.6 kW/cm² do we resolve the characteristic spectral shift of mixed halide perovskite halide phase segregation on the timescale relevant to the KPFM measurements in this work.[31] This suggests that any light-induced effect of halide phase segregation is negligible at the light intensity used here and that step III is of a different origin. Collins et al. have previously observed a similarly slow effect in FA-rich systems under external voltage.[32] The dynamics they
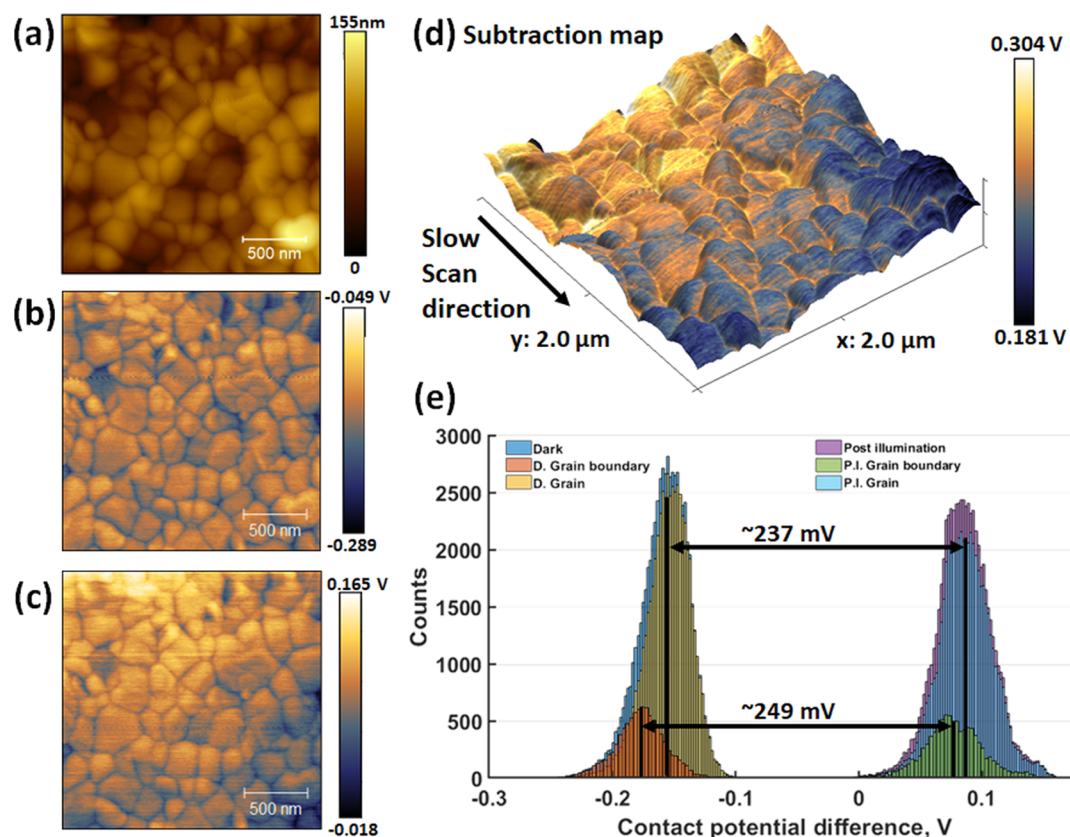

Figure 3. Initial dark and relaxed closed-loop KPFM analysis of CsFAMAPbBrI. (a) Topography channel plotting surface height. (b) KPFM image prior to light pulse plotting V_{cpd}. (c) KPFM image seconds after the light pulse plotting V_{cpd}. (d) 3D topography overlaid with the calculated ΔV_{cpd} map. (e) Histograms of before and after V_{cpd} maps separated into grain and GB responses. The double arrows indicate the difference between the mean values of the distributions.
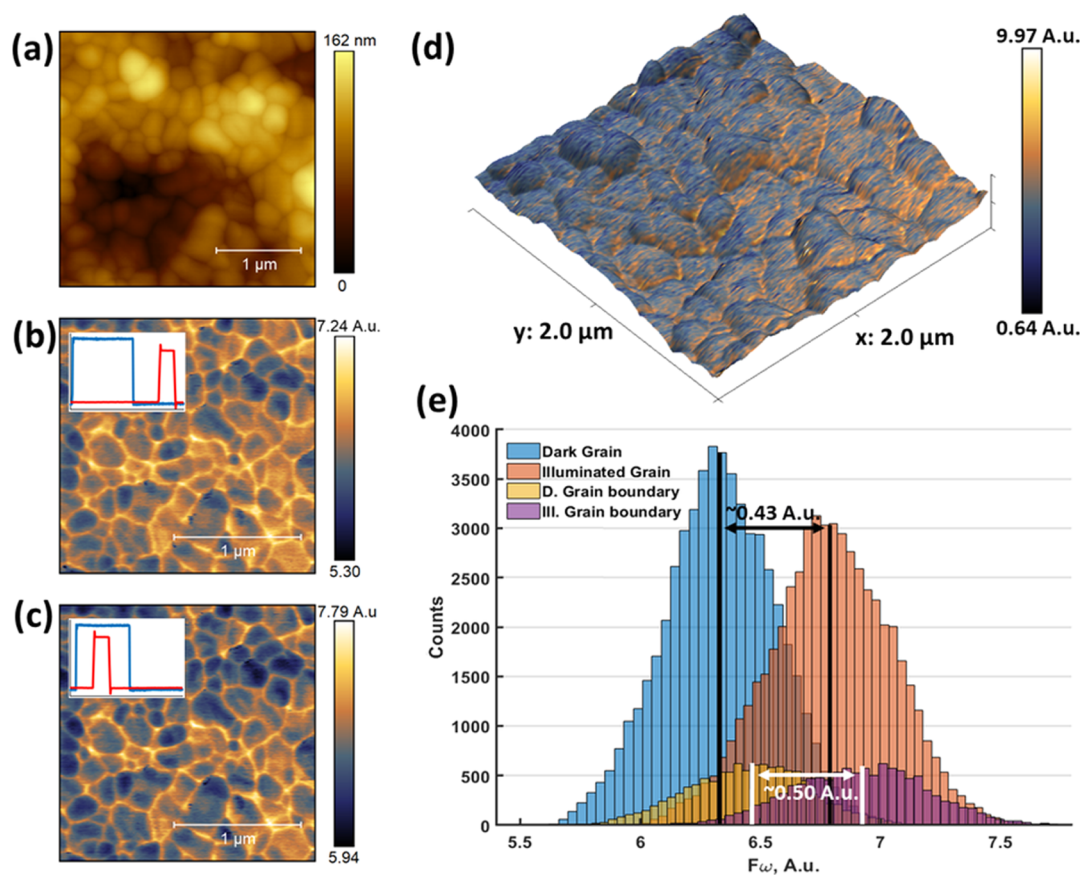
Figure 4. Open-loop pp-KPFM maps of mixed-halide CsFAMA at 150 kHz pulse frequencies: (a) Topography channel plotting surface height, (b) $F_{\omega,\text{off}}$ (in the dark) and (c) $F_{\omega,\text{on}}$ (under illumination). Insets in (b,c) show the pulse positions corresponding to the plots, where blue is the pump signal and red is the probe signal. (d) Topography overlaid with the difference of the light and dark F_ω signals. (e) Histograms of the pp-KPFM maps separated into grain and GB responses separated by grain segmentation.

observed were attributed to slow migration and accumulation of the organic cations. Accumulation of ions could also result in a change of the $F_{2\omega}$ component, which is related to dC/dz. By recording both F_ω and $F_{2\omega}$ signals in a dual-harmonic fashion (shown in Figure S2) according to Collins et al., we show that the dynamics of step III can be seen in both V_{cpd} and dC/dz, indicating a complex interplay of surface charges and capacitance change.[33] After turning off the illumination, we first observe a fast recombination of electron−hole pairs at a timescale of nanoseconds to microseconds (step IV) and then a relaxation takes place (step V) with similar dynamics to the charge accumulation in step III ($\tau_V = 4.24 \pm 0.19$ s) indicating a reversible process.

Charge Accumulation and Ionic Processes. To further investigate the charge accumulation and relaxation shown in steps III and V, we employed conventional KPFM mapping prior to and post illumination. Figure 3a shows the measured topography of the CsFAMAPbBrI sample deposited on ITO. The image shows varying grain sizes with 100−500 nm diameter and an overall mean roughness of ∼15 nm. The KPFM scan taken under dark conditions (Figure 3b) exhibits an average $V_{\text{cpd}} \sim -160$ mV with respect to the Au-coated tip. The measured V_{cpd} is directly related to the work functions of the AFM probe and the sample, $V_{\text{cpd}} = (\varphi_{\text{sample}} - \varphi_{\text{tip}})/e$, where φ_{sample} and φ_{tip} are the sample and tip work function, respectively, and e is the elementary charge. Thus, the contrast between grains and GBs in Figure 3b indicates a shallower work function at the GBs and therefore a downward band

bending toward the GBs. To probe the contribution of trapped charges to the slow accumulation and relaxation processes, we scanned the same area (within a few seconds) after an illumination period of ∼7 min with a confocal beam at an intensity of 1.05 kW/cm². A higher illumination intensity was employed for the measurements to give a sufficiently high photoinduced signal that the imaging could be completed within the relaxation timescale corresponding to step V in Figure 2. Figure 3c shows the KPFM image taken after the illumination, where mobile electron−hole pairs have completely recombined; thus, flattening of the bands at the perovskite−ITO interface can be disregarded. After illumination, the average sample potential is $V_{\text{cpd}} \sim 85$ mV with respect to the probe. From the difference of the two maps, we deduce the contribution of the trapped charges which results in the mean positive shift of $\Delta V_{\text{cpd}} = 243$ mV. The shift of V_{cpd} can be attributed to either a change in the sample work function or an accumulation of charges at the surface. As the electronic charge carriers have already recombined at the time of this measurement, a change in the sample work function is not expected; thus, we interpret the results as relaxation of negative charges at the top surface. In Figure 3d, we show the corresponding ΔV_{cpd} map overlaid on the surface topography, where a larger ΔV_{cpd} can be seen at the GBs. To compare the overall shift in V_{cpd} for different areas of the sample, we prepared a mask of the GBs from the flattened topography image using a classical Vincent algorithm for watersheds in digital spaces implemented in the open source Gwyddion
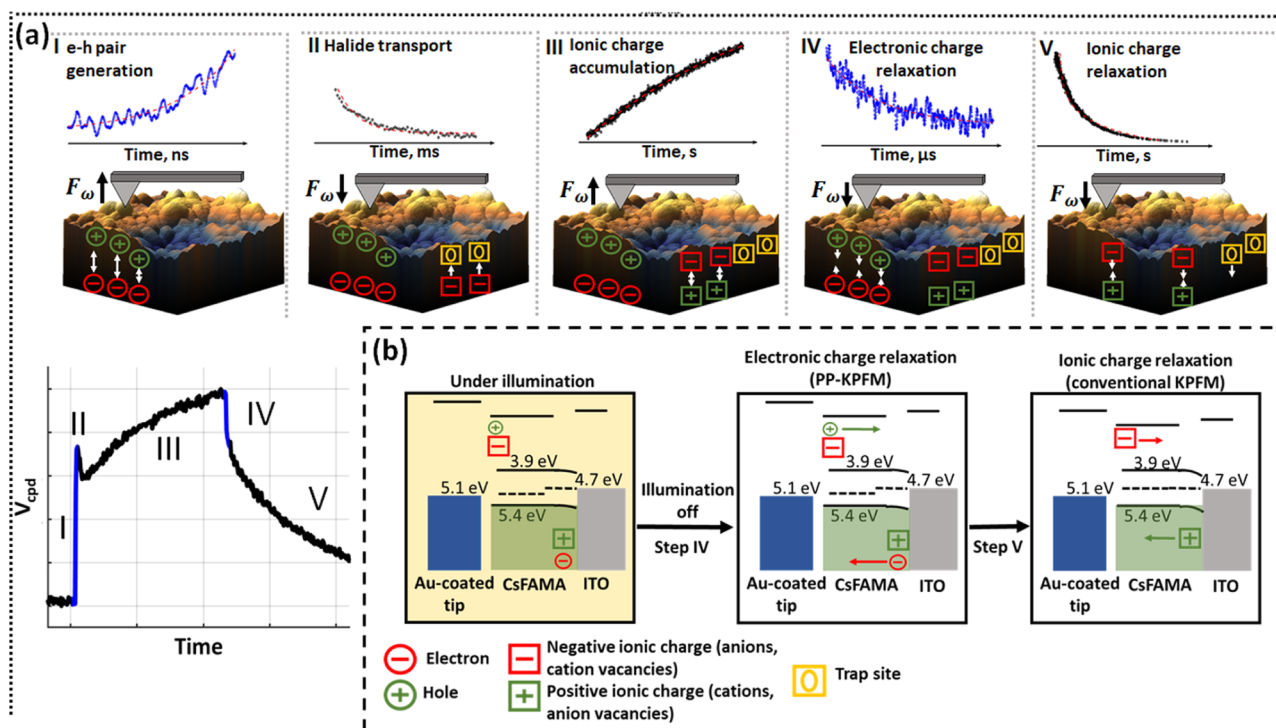
Figure 5. Detailed picture of electrostatic force response of mixed-halide CsFAMA. (a) Stepwise explanation of charge carrier transport from the electrostatic force response. (b) Band diagrams under illumination and for the two applied KPFM modes.

software (shown in Figure S3) and used this to separate datapoints at grains and GBs.[34] This type of analysis indicates that the light-induced change in V_{cpd} at the GBs (~249 mV) is higher than that observed on the grains (~237 mV) (Figure 3e). A similar slow transient was observed at the GBs after illumination and electrical polling in a different composition perovskite system.[35] Another important observation from Figure 3d is that the overlaid map exhibits a continuous change of ΔV_{cpd} over time under dark conditions during the measurement, which manifests as an overall gradient in ΔV_{cpd} along the slow scanning direction; this effect can be directly related to step V already described in Figure 2. Although the stability of the PL peak position shown in Figure S1 indicates reduced halide ionic movement, the contribution of other ions (e.g., MA^+, FA^+, etc.) and the corresponding charge trapping/detrapping at the nanoscale cannot be completely excluded from the observed effect.[15,36]

Open-Loop Pump–Probe KPFM. While the local dynamics of the trapped charges and ions are slow enough to be measured by standard KPFM, the much faster electronic charge carrier recombination and diffusion requires a different approach. Here, we employed open-loop pump–probe KPFM (pp-KPFM) to increase the temporal resolution. Briefly, in open-loop pp-KPFM, two high-frequency pulse signals with changing phase difference are applied to probe and light source, respectively, in order to resolve changes in the F_ω signal with high temporal resolution. In our approach, we used modulated laser pulses as the pump signal and a sinusoidally modulated pulse waveform applied to the tip as the probe signal and recorded F_ω as described in the Methods section. Additional details of this approach can be found in the Supporting Information. Pulse frequencies in the range of 50–150 kHz were selected to enable monitoring of microsecond timescale effects whilst still being modulatable by a sinusoidal

waveform at the cantilever resonance frequency, which improves sensitivity of detection. In Figure S4a, we present a typical open-loop pp-KPFM response from the perovskite layer and the dependence of the extracted time constants on the probe pulse-width. The applied probe pulse-width was varied to find the optimum pulse width, where the temporal resolution allowed us to resolve the sample response (Figure S4b).

With the previously described measurement parameters, we observed a ~1.8 μs relaxation and a ~1.3 μs generation time constant. Although ionic motion has been proposed to happen at tens of microsecond timescale, the observed time constant in our experiments is expected to be governed by electronic charge carrier diffusion and recombination.[17] Considering this, the asymmetry in the square response can be explained as the effect of nonradiative recombination and/or charge carrier diffusion times.[5] As such, the generation time constant is likely dominated by the probing pulse-width. After identifying the relaxation time constant of interest, we obtained open-loop pp-KPFM images of the CsFAMAPbBrI at the two different pulse positions indicated in the inset of Figure 4b,c. By subtraction of these maps we gain a high-frequency electrostatic force image that is directly related to the change in V_{cpd} for the sample at the timescale of the applied pulses (150 kHz), representing measurement in the dark and under illumination. Figure 4d shows the topography overlaid with the calculated difference. The result of the subtraction suggests heterogeneity among grains and, more importantly, a larger change at the GBs of the structures. Masking of the flattened topography (Figure S5) and calculation of the grain and GB histograms confirms this observation, as can be seen in Figure 4e. In order to exclude any effects of degradation because of the high dose of light exposure during the time between taking the two images, we repeated the measurements with a lower
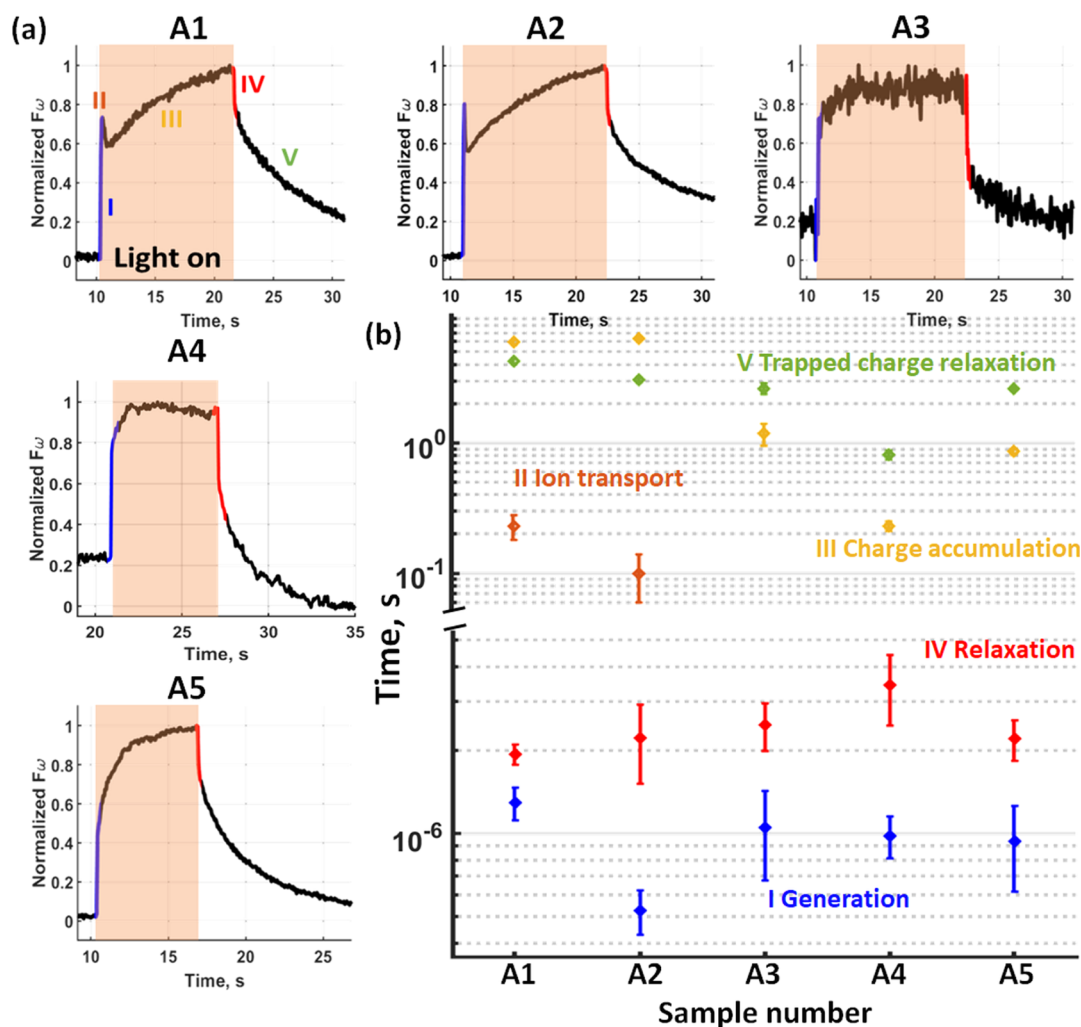
Figure 6. Carrier dynamics of multilayer CsFAMAPbBrI structures. (a) F_ω (open-loop KPFM) time response to a single light pulse for different multilayer structures. (b) Time constants extracted from each shown step and from pump−probe responses for the different samples. The characterized samples had the following layers deposited on glass/ITO: A1 perovskite, A2 NiO$_x$/perovskite, A3 NiO$_x$/perovskite/PCBM, A4 NiO$_x$/perovskite/PCBM/TiO$_x$ (10−15 nm), A5 NiO$_x$/perovskite/PCBM/TiO$_x$ (40−50 nm). The blue and red regions of the time traces correspond to the electron−hole pair generation and relaxation, respectively.

illumination intensity of 1 sun (Figure S6). These measurements showed the same contrast, confirming that the observed effect is not due to light induced degradation of the perovskite.

We interpret these findings as a larger change in potential because of a higher occurrence of charge relaxation events at the GBs over the course of ∼6.7 μs for the applied 150 kHz pulse frequency. Although the effect of GBs on charge carrier lifetime is still actively researched, our results show a clear difference in recombination dynamics between grains and GBs. The observed contrast might represent an increase in the rate of charge relaxation events at the GBs because of the presence of defect sites as has been observed before.[37−39] Alternatively, we note that the contrast in Figure 4d could indicate a difference in diffusion of charge carriers at the timescale of the applied pulses.

Combined Model of the CsFAMAPbBrI Response. The described effects can be summarized as follows: Figure 5b shows the band alignment of the structure. The work function of ITO is around 4.7 eV, the conduction and valence band edges of the perovskite are reported to be ∼3.9 and ∼5.4 eV, respectively, while the work function of the Au coated tip can be considered to be around 5.1 eV.[16,40,41] According to the

band diagram, the generated holes will preferentially move away from the perovskite−ITO interface upon illumination.

Thus, as shown in Figure 5a at step I, we resolve the movement of holes toward the top surface confirmed by the V_{cpd} shift in Figure 3. Intrinsically under dark conditions, the work function of the GBs is shallower, indicating a downward band bending toward the GBs. Previous studies proposed intrinsic iodide-rich regions in mixed-cation perovskites at GBs, which are responsible for the collection of photoinduced charge carriers.[37,38,42,43] Our open-loop pump−probe KPFM imaging measurements indicate diffusion of charge carriers toward the GBs with faster recombination dynamics that can be due to localized interstitial, vacancy, or antisite defects.[39] Consequently, after the electron−hole pair separation and charge localization at the GBs, negatively charged halide motion occurs toward the top surface in step II. At step III, negative charge carriers accumulate at GBs as shown in the ΔV_{cpd} map. The second timescale of this effect indicates ionic origin. Afterward, turning off the illumination results in a more negative potential at this interface because of electron−hole recombination (step IV). Finally, through relaxation of the trapped charges, the contact potential difference reaches a

more negative value close to the initial V_{cpd} (step V). One would expect a converse relaxation effect to the observed halide ionic motion (step II) in the time response, which was not observed for the measurements. Considering the higher magnitude of step V, we propose that it is overlapped by the relaxation of slower ionic charges. Previously, it has been shown that the activation energy of the halide motion is significantly higher under dark conditions.[44] Furthermore, Weber et al. have observed a ∼40 times slower relaxation of ion dynamics compared to the initial photoinduced displacement.[45] Although the conditions of the latter example differ from our measurement conditions, a combination of the described effects can result in this relaxation process to overlap with the larger magnitude step V in our measurements.

Application to Multilayer Structures. After describing the response of the perovskite, we apply the same approach to multilayer structures to investigate the effect of transport layers. Addition of a thin TiO_x layer on top of PCBM in an inverted configuration has shown an increase of charge extraction efficiency and improved optical properties.[16] The structure of the measured multilayer architectures can be found in the caption of Figure 6. First, in Figure 6a we show the electrostatic response to an illumination pulse for the different structures. The evaluation of the time constants and associated uncertainties bars is detailed in the Methods section. Table S1 contains the extracted parameters from the resulting monoexponential fits to the separate dynamical processes. Qualitative comparison of the responses shows that by depositing the perovskite on a hole-transport material, the previously described fast ionic motion (step II) and slow accumulation (step III) are amplified and accelerated. This can be explained by the extraction of holes into the NiO_x, leaving excess electrons in the perovskite.

A number of studies have shown a direct link between electron density and the promotion of ion diffusion through electron−phonon coupling and vacancy polarization.[36,44,46−48] Considering passivation of halide vacancies by electrons, the absence of step II for structures with ETM on top (A3−A4−A5) thus corroborates its ionic origin. Additionally, the surface charge accumulation was accelerated as seen in the extracted fitting time constant in Figure 6b for steps III and V. These observations are consistent with other studies showing that the addition of PCBM on the perovskite active layer results in passivation of shallow and deep traps.[1,49−51] The results indicate that the issues of charge accumulation or enhanced ion migration at the GBs can be resolved by appropriate surface passivation.[49] The addition of a thin TiO_x top layer results in a clear increase in the rate of charge accumulation and relaxation (steps III and V). On the other hand, a thicker TiO_x layer decreases the rate, which we attribute to reduced electronic conductivity. Application of the open-loop pump−probe KPFM approach confirms this observation. Figure 6b includes the extracted generation and relaxation times from single point time trace measurements. Clearly, in the cases with the perovskite top layer (A1, A2), we do not resolve significant differences in the fast charge carrier relaxation times. In cases with the ETMs on top of the active layer, the relaxation time increases, indicating a longer charge carrier diffusion time and/or recombination time. This can be due to interfacial energy barriers or an increase in trap-mediated recombination. This trend continues for the thin TiO_x layer. However, the samples with a 40−50 nm thick TiO_x layer showed a ∼1 μs decrease in the relaxation time. This result indicates an increased rate of

recombination or a decrease in the overall diffusion length of the charge carriers. As the macroscale IV and power conversion efficiency (PCE) measurements showed higher fill factor and PCE for the thin TiO_x capping layer compared to the thick, we propose that this is due to a high density of formed trap sites in the imperfect top layer.[16] As access only to the top layer of the device limits the characterization of layer specific mechanism, in order to understand the complete nanoscale effect of the double ETM structure, further time-resolved KPFM measurements on cross-sectional structures could provide a deeper understanding for the observed effects.

■ CONCLUSIONS

In conclusion, we applied KPFM techniques to characterize the charge carrier dynamics of mixed-cation mixed-halide perovskite $(Cs_{0.05}(FA_{0.83}MA_{0.17})_{0.95}PbI_{3−x}Br_x)$ structures under light excitation. Conventional EFM/KPFM measurements allowed us to separate light-induced effects of different timescales such as the charge carrier lifetimes and trapped charge relaxations. KPFM mapping revealed charge accumulation and trapped charge relaxation at the GBs with dynamics in the order of seconds (τ_{III} = 5.9 ± 0.2 s). Pump−probe implementation of open-loop KPFM revealed higher activity at the GBs indicating diffusion of charge carriers toward the GBs and faster local recombination. From our results and the corresponding literature, we have outlined a combined model for mixed-halide CsFAMA charge carrier dynamics that encompasses the spatially distributed nanoscale electric effects. This model can facilitate targeted use of the mechanisms described for advanced optoelectronic applications. Furthermore, the nanoscale charge dynamics of multilayer structures were measured by KPFM, showing a direct correlation with macroscale electrical and optical measurement results. Further investigation of these characteristics by advanced SPM techniques will direct progress in perovskite fabrication as well as optimized transport layer preparation. Finally, we highlight that the methodologies for nanoscale investigation of carrier dynamics employed here can be readily transferred to other research fields including advanced optoelectronic applications of 2D materials and optically active molecules in life science applications.[52,53]

■ METHODS

AFM Measurements. Two separate AFM setups were used for KPFM characterization. Measurements presented in the Supporting Information were taken on a Keysight Technologies 5600 large stage microscope in ∼1% relative humidity conditions. A modulatable CW 405 nm laser diode was used as the illumination source. Demodulation of the photodetector signal was done with the internal lock-in amplifiers of the AFM setup using 100 Hz bandwidth. Resonance frequency (13 kHz, PtSi-CONT, Nanosensors) silicon AFM tips with PtSi coating were used for these measurements. Square wave and pulse waveform generation was done with a Keysight Technologies 33500b series waveform generator. Rising and falling edges of the generated pulses were 2.9 ns across the complete modulation depth. The pump−probe measurements were performed keeping a constant 10 nm distance above the surface. The experiments were performed in an amplitude-modulated 2-pass KPFM manner.

Results presented in the main figures were taken on an AIST-NT CombiScope 1000 AFM system in a nitrogen atmosphere. For excitation, a 633 nm He−Ne laser was used, modulated by a New Focus 4102NF electro-optical modulator. For these measurements, 70 kHz nominal resonance frequency gold coated tips were employed. Imaging was done in lift mode keeping 10 nm distance with respect to

the topography pass. Tapping excitation of the probe was switched off in the second pass. The DC bias voltage was applied to the tip during the KPFM measurements. To avoid confusion of voltage polarities, we only present V_{cpd} data in the article, where the sign correction as described in Supporting Information Note S1 has already been applied. We note that the AFM measurements reported included rigorous efforts to minimize and remove any light-induced topographical change and photothermal cantilever bending by positioning of the illumination spot. This was done by monitoring the deflection and topography signals without any applied voltage to the probe and minimizing the effect of the illumination. Additionally, positioning of the laser beam and application of band pass optical filters allowed us to avoid any crosstalk in the laser read-out signal because of the applied laser illumination. As amplitude-modulated KPFM is prone to crosstalk from capacitive coupling and averaging due to the cantilever geometry, a series of measurements was done on the perovskite system at different lift heights shown in Figure S7. The results of this measurements demonstrate that the contrast shown in Figures 3 and 4 is due to local variation of V_{cpd} rather than a crosstalk artifact.

PL Measurements. Spectrally resolved PL was measured using a HORIBA Labram Evolution HR800 system. For optical excitation, a 633 nm He—Ne laser was used. A 300 lines/mm grating was used for spectral dispersion.

Fabrication of Perovskite Structures. Glass substrates coated with ITO (15 Ω/cm^2), lead iodide (PbI$_2$, Sigma-Aldrich, 99.9%), lead bromide (PbBr$_2$, Sigma-Aldrich, 99.99%), PCBM (Solenne BV), cesium iodide (CsI, Sigma-Aldrich, 99.99%), formamidine acetate salt (HN=CHNH$_2$·CH$_3$COOH, Sigma-Aldrich, 99%), hydroiodic acid (57 wt % in H$_2$O), hydrobromic acid (57 wt % in H$_2$O), methylamine (CH$_3$NH$_2$, Aldrich, 33 wt % in absolute ethanol), N,N-dimethylformamide (DMF, anhydrous, Sigma-Aldrich), dimethylsulfoxide (DMSO, Anal. R. VWR chemicals, 99.5%), and chlorobenzene were used as purchased. Nickel chloride hexahydrate (NiCl$_2$·6H$_2$O, Sigma-Aldrich, 99.9%) and sodium hydroxide (NaOH, Sigma-Aldrich, > 98%) were used to synthesize NiO$_x$ nanoparticles following the procedure reported by Yin et al.[54] To synthesize TiO$_x$ sol—gel, titanium(IV) isopropoxide (Ti[OCH(CH$_3$)$_2$]$_4$, Sigma-Aldrich, 99.9+ %), 2-methoxyethanol (CH$_3$OCH$_2$CH$_2$OH, Sigma-Aldrich, 99.9%), isopropanol (IPA), and ethanolamine (H$_2$NCH$_2$CH$_2$OH, Sigma-Aldrich, 99%) were used. TiO$_x$ sol—gel and organic salts [CH$_3$NH$_3$Br and CH(NH$_2$)$_2$I] were synthesized following the same synthesis procedure mentioned before.[16] The prepared perovskite film thickness was determined to be 500—550 nm using a profilometer. The five measured perovskite structures consisted of the perovskite directly deposited on glass substrates coated with ITO, the perovskite placed on glass/ITO/nickel-oxide, a glass/ITO/NiO$_x$/perovskite/PCBM structure, and glass/ITO/NiO$_x$/perovskite/PCBM/TiO$_x$ with different thicknesses of titanium oxide from 10 to 50 nm. Here, we refer to these as A1, A2, A3, A4, and A5, respectively. To prepare the samples, glass substrates coated with ITO were sequentially cleaned in acetone, detergent, deionized water, and IPA. NiO$_x$ particles (20 mg/mL in water) were cracked using an ultrasound sonicator (UP50H, 50 W, frequency 30 kHz), followed by filtration through a 0.45 μm pore-size polytetrafluoroethylene syringe filter. The filtrate dispersion was spin-coated on the ITO-coated substrate at 4000 rpm for 30 s. Then, the film was annealed at 140 °C for 20 min. For the deposition of perovskite films and further processing, the substrates were transferred into a glovebox. Triple-cation mixed-halide perovskite [Cs$_{0.05}$(FA$_{0.83}$MA$_{0.17}$)$_{0.95}$PbI$_{3-x}$Br$_x$] solution was prepared by dissolving PbI$_2$ (507.5 mg), CH(NH$_2$)$_2$I (172 mg), PbBr$_2$ (73.5 mg), and CH$_3$NH$_3$Br (22.4 mg) in a mixture of DMF and DMSO solvents (4:1 (v/v) ratio), followed by stirring at 45 °C. Then, 5% (v/v) of CsI (1.5 M in DMSO) was added into the mixture and stirred for about 3 h. The perovskite solution was deposited on top of ITO substrates to prepare S1 and ITO/NiO$_x$ films to fabricate S2, S3, S4, and S5. Spin-coating was conducted in two steps at 1500 rpm for 10 s with ramp: 150 rpm/s and at 6000 rpm for 30 s with ramp: 3000 rpm/s, with in situ antisolvent quenching by dropping about 0.15 mL of chlorobenzene for about 3 s. The films were annealed at 100 °C for 1 h. Then, films were cooled to room temperature. To prepare S3,

S4, and S5, PCBM dissolved in a mixture of chlorobenzene and chloroform (50:50 volume ratio, 2 wt %) was spin-coated on top of the perovskite films. Diluted TiO$_x$ sol—gel solution was spin-coated on top of PCBM at 5000 rpm for 30 s for S4 and at 3000 rpm for 30 s to finish S5, followed by annealing at 110 °C for about 5 min in ambient air.

Extraction of Time Constants. A custom Wolfram Mathematica script was used for the extraction of time constants from the pump—probe responses utilizing a Heaviside function with exponential rising and falling edges. The defined function was fitted to six periods of the recorded signal. In Figure S4a, a mean value of the resulting corrected time constant is presented with the standard deviation. Time constants from the low-frequency single-light pulse responses were extracted from monoexponential fitting in Origin. Data shown in Figure S4b represents the extracted time constants with the error resulting from the fit.

■ ASSOCIATED CONTENT

Ⓢ Supporting Information

The Supporting Information is available free of charge at https://pubs.acs.org/doi/10.1021/acsami.0c10641.

> PL response of the mixed halide CsFAMA perovskite, first- and second-harmonic of the electrostatic force as well as calculated contact potential difference response to an illumination pulse, mask generated from the topographical data shown in Figure 3, a recorded pump—probe KPFM time trace with variation of extracted time constant versus probing pulse width, mask generated from topographical data for Figure 5, results of pump—probe open-loop KPFM measured under 633 nm, ~0.1 W/cm^2 illumination intensity, closed-loop KPFM measurements to exclude capacitive crosstalk from imaging data, exponential fit parameters extracted from single-light pulse responses, and KPFM, pp-KPFM, and its application (PDF)

■ AUTHOR INFORMATION

Corresponding Author

Georg Gramse — *Keysight Technologies GmbH, Linz 4020, Austria; Applied Experimental Biophysics, Johannes Kepler University, Linz 4020, Austria;* Email: georg.gramse@jku.at

Authors

David Toth — *Keysight Technologies GmbH, Linz 4020, Austria; Applied Experimental Biophysics, Johannes Kepler University, Linz 4020, Austria;* Ⓞ orcid.org/0000-0002-9875-8615

Bekele Hailegnaw — *Linz Institute for Organic Solar Cells (LIOS), Johannes Kepler University, Linz 4020, Austria;* Ⓞ orcid.org/0000-0003-4427-2772

Filipe Richheimer — *National Physical Laboratory, Teddington TW11 0LW, U.K.*

Fernando A. Castro — *National Physical Laboratory, Teddington TW11 0LW, U.K.*

Ferry Kienberger — *Keysight Technologies GmbH, Linz 4020, Austria*

Markus C. Scharber — *Linz Institute for Organic Solar Cells (LIOS), Johannes Kepler University, Linz 4020, Austria;* Ⓞ orcid.org/0000-0002-4918-4803

Sebastian Wood — *National Physical Laboratory, Teddington TW11 0LW, U.K.*

Complete contact information is available at:
https://pubs.acs.org/10.1021/acsami.0c10641

REFERENCES

(1) Wang, R.; Mujahid, M.; Duan, Y.; Wang, Z. K.; Xue, J.; Yang, Y. A Review of Perovskites Solar Cell Stability. *Adv. Funct. Mater.* **2019**, *29*, 1808843.

(2) Hidalgo, J.; Castro-Méndez, A. F.; Correa-Baena, J. P. Imaging and Mapping Characterization Tools for Perovskite Solar Cells. *Adv. Energy Mater.* **2019**, *9*, 1900444.

(3) Wang, H.; Guerrero, A.; Bou, A.; Al-Mayouf, A. M.; Bisquert, J. Kinetic and Material Properties of Interfaces Governing Slow Response and Long Timescale Phenomena in Perovskite Solar Cells. *Energy Environ. Sci.* **2019**, *12*, 2054−2079.

(4) Yang, T. C.-J.; Fiala, P.; Jeangros, Q.; Ballif, C. High-Bandgap Perovskite Materials for Multijunction Solar Cells. *Joule* **2018**, *2*, 1421−1436.

(5) Knight, A. J.; Wright, A. D.; Patel, J. B.; McMeekin, D. P.; Snaith, H. J.; Johnston, M. B.; Herz, L. M. Electronic Traps and Phase Segregation in Lead Mixed-Halide Perovskite. *ACS Energy Lett.* **2019**, *4*, 75−84.

(6) Knight, A. J.; Patel, J. B.; Snaith, H. J.; Johnston, M. B.; Herz, L. M. Trap States, Electric Fields, and Phase Segregation in Mixed-Halide Perovskite Photovoltaic Devices. *Adv. Energy Mater.* **2020**, *10*, 1903488.

(7) deQuilettes, D. W.; Zhang, W.; Burlakov, V. M.; Graham, D. J.; Leijtens, T.; Osherov, A.; Bulović, V.; Snaith, H. J.; Ginger, D. S.; Stranks, S. D. Photo-Induced Halide Redistribution in Organic−Inorganic Perovskite Films. *Nat. Commun.* **2016**, *7*, 11683.

(8) Gualdrón-Reyes, A. F.; Yoon, S. J.; Barea, E. M.; Agouram, S.; Muñoz-Sanjosé, V.; Meléndez, Á. M.; Niño-Gómez, M. E.; Mora-Seró, I. Controlling the Phase Segregation in Mixed Halide Perovskites through Nanocrystal Size. *ACS Energy Lett.* **2019**, *4*, 54−62.

(9) Chen, S.; Hou, Y.; Chen, H.; Tang, X.; Langner, S.; Li, N.; Stubhan, T.; Levchuk, I.; Gu, E.; Osvet, A.; Brabec, C. J. Exploring the Stability of Novel Wide Bandgap Perovskites by a Robot Based High Throughput Approach. *Adv. Energy Mater.* **2018**, *8*, 1701543.

(10) Wang, Y.; Hu, Z.; Gao, C.; Yang, C.; Zhang, J.; Zhu, Y. Comprehensive Elucidation of Grain Boundary Behavior in All-Inorganic Halide Perovskites by Scanning Probe Microscopy. *Adv. Mater. Interfaces* **2020**, *7*, 1901521.

(11) Si, H.; Zhang, S.; Ma, S.; Xiong, Z.; Kausar, A.; Liao, Q.; Zhang, Z.; Sattar, A.; Kang, Z.; Zhang, Y. Emerging Conductive Atomic Force Microscopy for Metal Halide Perovskite Materials and Solar Cells. *Adv. Energy Mater.* **2020**, *10*, 1903922.

(12) Li, J.; Huang, B.; Nasr Esfahani, E.; Wei, L.; Yao, J.; Zhao, J.; Chen, W. Touching Is Believing: Interrogating Halide Perovskite Solar Cells at the Nanoscale via Scanning Probe Microscopy. *npj Quantum Mater.* **2017**, *2*, 56.

(13) Li, J.-J.; Ma, J.-Y.; Ge, Q.-Q.; Hu, J.-S.; Wang, D.; Wan, L.-J. Microscopic Investigation of Grain Boundaries in Organolead Halide Perovskite Solar Cells. *ACS Appl. Mater. Interfaces* **2015**, *7*, 28518−28523.

(14) Tennyson, E. M.; Roose, B.; Garrett, J. L.; Gong, C.; Munday, J. N.; Abate, A.; Leite, M. S. Cesium-Incorporated Triple Cation Perovskites Deliver Fully Reversible and Stable Nanoscale Voltage Response. *ACS Nano* **2019**, *13*, 1538.

(15) Beal, R. E.; Hagström, N. Z.; Barrier, J.; Gold-Parker, A.; Prasanna, R.; Bush, K. A.; Passarello, D.; Schelhas, L. T.; Brüning, K.; Tassone, C. J.; Steinrück, H.-G.; McGehee, M. D.; Toney, M. F.; Nogueira, A. F. Structural Origins of Light-Induced Phase Segregation in Organic-Inorganic Halide Perovskite Photovoltaic Materials. *Matter* **2020**, *2*, 207−219.

(16) Hailegnaw, B.; Adam, G.; Heilbrunner, H.; Apaydin, D. H.; Ulbricht, C.; Sariciftci, N. S.; Scharber, M. C. Inverted (p−i−n) Perovskite Solar Cells Using a Low Temperature Processed TiO x Interlayer. *RSC Adv.* **2018**, *8*, 24836−24846.

(17) Collins, L.; Ahmadi, M.; Wu, T.; Hu, B.; Kalinin, S. V.; Jesse, S. Breaking the Time Barrier in Kelvin Probe Force Microscopy: Fast Free Force Reconstruction Using the G-Mode Platform. *ACS Nano* **2017**, *11*, 8717−8729.

(18) Almadori, Y.; Moerman, D.; Martinez, J. L.; Leclère, P.; Grévin, B. Multimodal Noncontact Atomic Force Microscopy and Kelvin Probe Force Microscopy Investigations of Organolead Tribromide Perovskite Single Crystals. *Beilstein J. Nanotechnol.* **2018**, *9*, 1695−1704.

(19) Giridharagopal, R.; Precht, J. T.; Jariwala, S.; Collins, L.; Jesse, S.; Kalinin, S. V.; Ginger, D. S. Time-Resolved Electrical Scanning Probe Microscopy of Layered Perovskites Reveals Spatial Variations in Photoinduced Ionic and Electronic Carrier Motion. *ACS Nano* **2019**, *13*, 2812−2821.

(20) Hermes, I. M.; Hou, Y.; Bergmann, V. W.; Brabec, C. J.; Weber, S. A. L. The Interplay of Contact Layers: How the Electron Transport Layer Influences Interfacial Recombination and Hole Extraction in Perovskite Solar Cells. *J. Phys. Chem. Lett.* **2018**, *9*, 6249−6256.

(21) Hamers, R. J.; Cahill, D. G. Ultrafast Time Resolution in Scanned Probe Microscopies. *Appl. Phys. Lett.* **1990**, *57*, 2031−2033.

(22) Jahng, J.; Brocious, J.; Fishman, D. A.; Yampolsky, S.; Nowak, D.; Huang, F.; Apkarian, V. A.; Wickramasinghe, H. K.; Potma, E. O. Ultrafast Pump-Probe Force Microscopy with Nanoscale Resolution. *Appl. Phys. Lett.* **2015**, *106*, 083113.

(23) Collins, L.; Belianinov, A.; Somnath, S.; Balke, N.; Kalinin, S. V.; Jesse, S. Full Data Acquisition in Kelvin Probe Force Microscopy: Mapping Dynamic Electric Phenomena in Real Space. *Sci. Rep.* **2016**, *6*, 30557.

(24) Grévin, B.; Bardagot, O.; Demadrille, R. Implementation of Data-Cube Pump−Probe KPFM on Organic Solar Cells. *Beilstein J. Nanotechnol.* **2020**, *11*, 323−337.

(25) Mogi, H.; Wang, Z.-h.; Kikuchi, R.; Hyun Yoon, C.; Yoshida, S.; Takeuchi, O.; Shigekawa, H. Externally Triggerable Optical Pump-Probe Scanning Tunneling Microscopy. *Appl. Phys. Express* **2019**, *12*, 025005.

(26) Collins, L.; Ahmadi, M.; Qin, J.; Liu, Y.; Ovchinnikova, O. S.; Hu, B.; Jesse, S.; Kalinin, S. V. Time Resolved Surface Photovoltage Measurements Using a Big Data Capture Approach to KPFM. *Nanotechnology* **2018**, *29*, 445703.

(27) Schumacher, Z.; Spielhofer, A.; Miyahara, Y.; Grutter, P. The Limit of Time Resolution in Frequency Modulation Atomic Force Microscopy by a Pump-Probe Approach. *Appl. Phys. Lett.* **2017**, *110*, 053111.

(28) Murawski, J.; Graupner, T.; Milde, P.; Raupach, R.; Zerweck-Trogisch, U.; Eng, L. M. Pump-Probe Kelvin-Probe Force Microscopy: Principle of Operation and Resolution Limits. *J. Appl. Phys.* **2015**, *118*, 154302.

(29) Sadewasser, S.; Nicoara, N.; Solares, S. D. Artifacts in Time-Resolved Kelvin Probe Force Microscopy. *Beilstein J. Nanotechnol.* **2018**, *9*, 1272−1281.

(30) Hoke, E. T.; Slotcavage, D. J.; Dohner, E. R.; Bowring, A. R.; Karunadasa, H. I.; McGehee, M. D. Reversible Photo-Induced Trap Formation in Mixed-Halide Hybrid Perovskites for Photovoltaics. *Chem. Sci.* **2015**, *6*, 613−617.

(31) Draguta, S.; Sharia, O.; Yoon, S. J.; Brennan, M. C.; Morozov, Y. V.; Manser, J. S.; Kamat, P. V.; Schneider, W. F.; Kuno, M. Rationalizing the Light-Induced Phase Separation of Mixed Halide Organic−Inorganic Perovskites. *Nat. Commun.* **2017**, *8*, 200.

(32) Collins, L.; Muckley, E. S.; Tsai, H.; Ghosh, D.; Neukirch, A. J.; Tretiak, S.; Kalinin, S. V.; Nie, W.; Ivanov, I. N. Correlation of Spatiotemporal Dynamics of Polarization and Charge Transport in Blended Hybrid Organic−Inorganic Perovskites on Macro- and Nanoscales. *ACS Appl. Mater. Interfaces* **2020**, *12*, 15380−15388.

(33) Collins, L.; Kilpatrick, J. I.; Weber, S. A. L.; Tselev, A.; Vlassiouk, I. V.; Ivanov, I. N.; Jesse, S.; Kalinin, S. V.; Rodriguez, B. J. Open Loop Kelvin Probe Force Microscopy with Single and Multi-Frequency Excitation. *Nanotechnology* **2013**, *24*, 475702.

(34) Vincent, L.; Soille, P. Watersheds in Digital Spaces: An Efficient Algorithm Based on Immersion Simulations. *IEEE Trans. Pattern Anal. Mach. Intell.* **1991**, *13*, 583−598.

(35) Yun, J. S.; Seidel, J.; Kim, J.; Soufiani, A. M.; Huang, S.; Lau, J.; Jeon, N. J.; Seok, S. I.; Green, M. A.; Ho-Baillie, A. Critical Role of Grain Boundaries for Ion Migration in Formamidinium and Methylammonium Lead Halide Perovskite Solar Cells. *Adv. Energy Mater.* **2016**, *6*, 1600330.

(36) Bischak, C. G.; Hetherington, C. L.; Wu, H.; Aloni, S.; Ogletree, D. F.; Limmer, D. T.; Ginsberg, N. S. Origin of Reversible Photoinduced Phase Separation in Hybrid Perovskites. *Nano Lett.* **2017**, *17*, 1028−1033.

(37) Doherty, T. A. S.; Winchester, A. J.; Macpherson, S.; Johnstone, D. N.; Pareek, V.; Tennyson, E. M.; Kosar, S.; Kosasih, F. U.; Anaya, M.; Abdi-Jalebi, M.; Andaji-Garmaroudi, Z.; Wong, E. L.; Madéo, J.; Chiang, Y.-H.; Park, J.-S.; Jung, Y.-K.; Petoukhoff, C. E.; Divitini, G.; Man, M. K. L.; Ducati, C.; Walsh, A.; Midgley, P. A.; Dani, K. M.; Stranks, S. D. Performance-Limiting Nanoscale Trap Clusters at Grain Junctions in Halide Perovskites. *Nature* **2020**, *580*, 360−366.

(38) Feldmann, S.; Macpherson, S.; Senanayak, S. P.; Abdi-Jalebi, M.; Rivett, J. P. H.; Nan, G.; Tainter, G. D.; Doherty, T. A. S.; Frohna, K.; Ringe, E.; Friend, R. H.; Sirringhaus, H.; Saliba, M.; Beljonne, D.; Stranks, S. D.; Deschler, F. Photodoping through Local Charge Carrier Accumulation in Alloyed Hybrid Perovskites for Highly Efficient Luminescence. *Nat. Photonics* **2020**, *14*, 123−128.

(39) Lee, J.-W.; Bae, S.-H.; De Marco, N.; Hsieh, Y.-T.; Dai, Z.; Yang, Y. The Role of Grain Boundaries in Perovskite Solar Cells. *Mater. Today Energy* **2018**, *7*, 149−160.

(40) Michaelson, H. B. The Work Function of the Elements and Its Periodicity. *J. Appl. Phys.* **1977**, *48*, 4729−4733.

(41) Nehate, S. D.; Prakash, A.; Mani, P. D.; Sundaram, K. B. Work Function Extraction of Indium Tin Oxide Films from MOSFET Devices. *ECS J. Solid State Sci. Technol.* **2018**, *7*, P87−P90.

(42) Zhang, B.; Guo, F.; Xue, J.; Yang, L.; Zhao, Y.; Ge, M.; Cai, Q.; Liu, B.; Xie, Z.; Chen, D.; Lu, H.; Zhang, R.; Zheng, Y. Photoluminescence Study of the Photoinduced Phase Separation in Mixed-Halide Hybrid Perovskite CH3NH3Pb(BrxI1−x)3 Crystals Synthesized via a Solvothermal Method. *Sci. Rep.* **2017**, *7*, 17695.

(43) Yoon, S. J.; Draguta, S.; Manser, J. S.; Sharia, O.; Schneider, W. F.; Kuno, M.; Kamat, P. V. Tracking Iodide and Bromide Ion Segregation in Mixed Halide Lead Perovskites during Photo-irradiation. *ACS Energy Lett.* **2016**, *1*, 290−296.

(44) Elmelund, T.; Seger, B.; Kuno, M.; Kamat, P. V. How Interplay between Photo and Thermal Activation Dictates Halide Ion Segregation in Mixed Halide Perovskites. *ACS Energy Lett.* **2020**, *5*, 56−63.

(45) Weber, S. A. L.; Hermes, I. M.; Turren-Cruz, S.-H.; Gort, C.; Bergmann, V. W.; Gilson, L.; Hagfeldt, A.; Graetzel, M.; Tress, W.; Berger, R. How the Formation of Interfacial Charge Causes Hysteresis in Perovskite Solar Cells. *Energy Environ. Sci.* **2018**, *11*, 2404−2413.

(46) Shahivandi, H.; Vaezzadeh, M.; Saeidi, M. Theory of Light-Induced Degradation in Perovskite Solar Cells. *Sol. Energy Mater. Sol. Cells* **2020**, *208*, 110383.

(47) Lin, Y.; Chen, B.; Fang, Y.; Zhao, J.; Bao, C.; Yu, Z.; Deng, Y.; Rudd, P. N.; Yan, Y.; Yuan, Y.; Huang, J. Excess Charge-Carrier Induced Instability of Hybrid Perovskites. *Nat. Commun.* **2018**, *9*, 4981.

(48) Braly, I. L.; Stoddard, R. J.; Rajagopal, A.; Uhl, A. R.; Katahara, J. K.; Jen, A. K.-Y.; Hillhouse, H. W. Current-Induced Phase Segregation in Mixed Halide Hybrid Perovskites and Its Impact on Two-Terminal Tandem Solar Cell Design. *ACS Energy Lett.* **2017**, *2*, 1841−1847.

(49) Chen, B.; Rudd, P. N.; Yang, S.; Yuan, Y.; Huang, J. Imperfections and Their Passivation in Halide Perovskite Solar Cells. *Chem. Soc. Rev.* **2019**, *48*, 3842−3867.

(50) Zhong, Y.; Hufnagel, M.; Thelakkat, M.; Li, C.; Huettner, S. Role of PCBM in the Suppression of Hysteresis in Perovskite Solar Cells. *Adv. Funct. Mater.* **2020**, *30*, 1908920.

(51) Li, S.; Fan, K.; Cui, Y.; Leng, S.; Ying, Y.; Zou, W.; Liu, Z.; Li, C.-Z.; Yao, K.; Huang, H. Unravelling the Mechanism of Ionic Fullerene Passivation for Efficient and Stable Methylammonium-Free Perovskite Solar Cells. *ACS Energy Lett.* **2020**, *5*, 2015−2022.

(52) Gramse, G.; Schönhals, A.; Kienberger, F. Nanoscale Dipole Dynamics of Protein Membranes Studied by Broadband Dielectric Microscopy. *Nanoscale* **2019**, *11*, 4303−4309.

(53) Gramse, G.; Kölker, A.; Lim, T.; Stock, T. J. Z.; Solanki, H.; Schofield, S. R.; Brinciotti, E.; Aeppli, G.; Kienberger, F.; Curson, N. J. Nondestructive Imaging of Atomically Thin Nanostructures Buried in Silicon. *Sci. Adv.* **2017**, *3*, No. e1602586.

(54) Yin, X.; Chen, P.; Que, M.; Xing, Y.; Que, W.; Niu, C.; Shao, J. Highly Efficient Flexible Perovskite Solar Cells Using Solution-Derived NiO x Hole Contacts. *ACS Nano* **2016**, *10*, 3630−3636.